Elliptic flow of deuterons in ultrarelativistic heavy-ion collisions

Radka Vozábová[1] and Boris Tomášik[1,2]

[1]*Faculty of Nuclear Sciences and Physical Engineering, Czech Technical University in Prague, Břehová 7, 11519 Prague 1, Czech Republic*
[2]*Univerzita Mateja Bela, Tajovského 40, 974 01 Banská Bystrica, Slovakia*

(Received 26 February 2024; accepted 9 May 2024; published 11 June 2024)

We calculate the elliptic flow of deuterons in Pb+Pb collisions at 2.76 TeV per colliding nucleon-nucleon pair and show that it can be used to discriminate between direct statistical production and coalescence. The emission from the fireball is parametrized and tuned to reproduce transverse momentum spectra and the elliptic flow of protons and pions. Coalescence leads to higher deuteron elliptic flow than statistical production and agrees better with experimental data. We attribute this observation to the varying size of the nucleon-producing region for the emission in different azimuthal angles.

DOI: 10.1103/PhysRevC.109.064908

I. INTRODUCTION AND MOTIVATION

Ultrarelativistic collisions of heavy atomic nuclei are examined with the aim to probe matter at the highest temperatures ever created in the laboratory. However, a few very interesting results have been achieved in parallel to the main line of research. One of them is the production of light nuclear clusters. Even very exotic ones have been identified among the produced particles, such as the antimatter $^4\overline{\mathrm{He}}$ nucleus [1] or the hypertriton as well as the antihypertriton [2]. Nevertheless, while these measurements were crucial for the understanding of the properties of the measured clusters, the results are still inconclusive regarding the mechanism of their production.

The inconclusivity occurs already at the level of the simplest nuclear clusters: deuterons and antideuterons. On one hand, the yields of deuterons, antideuterons, and heavier clusters alongside other types of hadrons including pions, kaons, and protons can all be reproduced by the statistical model [3,4] reasonably well. It seems as if the statistical model really provides a universal description for the bulk properties of matter reflected in hadron species and their clusters. At first sight, however, this is extremely puzzling, since the cluster binding energy is two orders of magnitude below the characteristic temperature, the former being a few MeV and the latter about 150 MeV. Quite naturally, production of deuterons from a system at such a high temperature has led to the metaphor "snowballs in hell" [3].

The results [3,5] show that both the statistical model and the coalescence mechanism predict similar deuteron yields. However, when using a blast-wave model as a representation of thermal production of the proton p_t spectra and v_2 and simply replacing the proton mass by those of light nuclei, the data on the elliptic flows of these light nuclei [6] are not well reproduced.

Coalescence is a natural mechanism for the deuteron and cluster production [7–21]. Due to their low binding energy it is assumed that the clusters are formed by coupling nucleons only after the latter have escaped the strongly interacting fireball.

The similarity of results from statistical production and coalescence is intriguing and it provokes a question if such an agreement of the different models is a robust feature based on underlying physics processes or mere coincidence resulting from fine tuning of a number of small contributing effects [22]. Even though a bound cluster cannot really be produced in a hot environment, an idea was put forward about an existence of correlated nucleon n-tuples already at high temperatures, that could later transform themselves into observed clusters [3].

Deuteron production was described in dynamical models a long time ago [23]. Current data are addressed in dynamical studies with transport models which focus on the microscopic production and survival of deuterons *within* the hot hadronic phase. Studies with SMASH [24,25] included destroying and regenerating scattering of deuterons, but ignored their very large formation time [26]. A newly constructed Parton-Hadron Quantum-Molecular Dynamics model (PHQMD) [27] includes direct interaction between baryons beyond the mean field and a cluster finding algorithm that identifies the clusters during the evolution of the hot hadronic phase. Experimental results on rapidity distributions and transverse momentum spectra were successfully reproduced for energies of few hundreds MeV up to 200 GeV per colliding NN pair [28–31]. It was shown that coalescence, which is applied only after the breakup of the hadronic phase, yields similar results for the deuterons [29]. A kinetic approach to production of lighter nuclei has also been applied for nucleon reactions at intermediate energies [32].

Due to the finite size of the deuteron, coalescence depends on the spatiotemporal extension of the source, which is measured by femtoscopy [12,33–35]. To more explicitly include this feature, a quantum-mechanical formalism of [14] was recently generalized [36]. Another extension, motivated also by the need to explain antideuteron production in collisions of cosmic ray particles, which are usually small systems, has also been worked out [37–39] and implemented for computation [40].

The constraint of coupling coalescence to the source sizes has been implemented in several analyses that aim at distinguishing the true production mechanism. Early simple estimates of the coalescence parameter [41] were later improved with a more advanced formalism [36,42] to the extent that the model deuteron wave function could be optimized to fit the experimental data best [43].

Other possibilities to discriminate between the two production models include examining the production of very exotic spatially extended and high spin isotope ^{4}Li [44], and/or performing femtoscopic studies involving correlations of deuterons to protons or other hadrons [45], or among themselves [46].

Recently, an enhancement of deuteron production within jet cones [47,48] was also successfully interpreted within the coalescence picture [49].

In [50], the cumulants of the deuteron number distribution were argued to be enhanced for coalescence with respect to the prediction from the statistical model. Measurements from ALICE [51] and STAR [52] Collaborations indicate a disagreement with the predictions from coalescence.

In this paper, we examine the idea of using v_2 measurements of deuterons for the distinction between coalescence and statistical production. The elliptic flow of deuterons from coalescence has been simulated before [5,53–56] but a comparison of the models has not been done. By doing so, we further explore the idea that deuterons from coalescence are a femtoscopic probe, i.e., their production is determined by the size of the homogeneity region from which their nucleons were produced. This is mostly the case if the homogeneity region is comparable to the typical size of the deuteron wave function, which is about 2 fm. Based on this, we suppose that the elliptic flow of deuterons may be a sensitive test of coalescence, because it measures the variations of deuteron yield in different azimuthal directions. Deuterons produced in different azimuthal directions are built from nucleons that originate from corresponding different homogeneity regions, which in noncentral collisions may differ by size. This may lead to the sensitivity of coalescence to the direction of deuteron production.

In a way, we propose to look at more detailed structure of the source than was done so far in studies of deuteron production. This will require devoting more attention to the modeling of the source, which we will constrain from hadronic observables.

For the actual calculation we use a model with a parametrized freeze-out hypersurface, including production of hadrons from decays of resonances, and implementing corrections to the momentum distribution function due to viscosity. The parametrization is based on an extension and upgrade of the blast-wave model. Our results indicate—in accordance with the reasoning above—that thermal production and coalescence indeed lead to different elliptic flows, provided that the fireball anisotropy is large enough.

We explain this approach in more detail in Sec. II. The model used here is introduced in Sec. III, together with its calibration. Our results are summarized in Sec. IV and we conclude in Sec. V. A technical description of the freeze-out implementation is placed in the Appendix.

II. THE APPROACH

In this paper we are interested in the mechanism of deuteron production, which happens at the kinetic freeze-out. We will not try to link that production to previous evolution of the bulk matter, its properties, and/or initial conditions. The reason is that we chose to look at differential v_2, which is statistics hungry in simulations. Thus, getting it from a dynamical simulation for various setups would easily become practically intractable. Also, we want the freedom to explore the production process at carefully chosen freeze-out while not making the approach more complicated than necessary. Therefore, we decided to use a *parametrization* of the kinetic freeze-out state of hadrons which we can tune with the help of a few parameters.

A representation of such a parametrization is the well-known blast-wave model. Here, we extend this model further in several aspects, guided by experimental data.

In the hadronic fireball, just before its kinetic freeze-out, nucleons and pions interact strongly with each others. In fact, pions are the mediators of nucleon-nucleon interaction. This leads us to assume that they decouple from the fireball at the same time and must be described by the same emission function, with a different mass inserted. This sets the constraint for our modeling of the kinetic freeze-out: we require that the model reproduces azimuthally integrated p_t spectra of protons and charged pions, as well as their v_2 as a function of p_t. During our work, it has turned out that the requirement to fit all these data of the two identified species fixes the parametrization rather uniquely.

Then, the subsequent calculation of the p_t distribution and the differential v_2 of the deuterons can be considered as a prediction, since there is basically no freedom to re-adjust the model, which has been set on protons and pions.

We can then directly generate the thermally produced deuterons; we just need to set the mass to that of the deuteron and use proper spin degeneracy factor.

Coalescence is simulated in two steps. The mechanism can be understood from the formula for the single-particle spectrum of deuterons [14],

$$E_d \frac{dN_d}{d^3P_d} = \frac{3}{8(2\pi)^3} \int_{\Sigma_f} P_d \cdot d\Sigma_f(R_d) \times f_p\left(R_d, \frac{P_d}{2}\right) f_n\left(R_d, \frac{P_d}{2}\right) \mathcal{C}_d(R_d, P_d), \quad (1)$$

where we use $a \cdot b = a_\mu b^\mu$ for the scalar product and the factor $\mathcal{C}_d(R_d, P_d)$ represents

$$\mathcal{C}_d(R_d, P_d) = \int \frac{d^3q d^3r}{(2\pi)^3} \frac{f_p(R_+, P_+) f_n(R_-, P_-)}{f_p(R_d, P_d/2) f_n(R_d, P_d/2)} \mathcal{D}(\vec{r}, \vec{q}). \quad (2)$$

The integration in Eq. (1) runs over the kinetic freeze-out hypersurface, $d\Sigma_f(R_d)$ is the surface element along the hypersurface, and R_d marks a position on that hypersurface, ascribed to the deuteron. Distributions of protons and neutrons in phase space are denoted f_p and f_n. The actual mechanism of coalescence is represented by the factor $\mathcal{C}_d(R_d, P_d)$. The integration in Eq. (2) runs over relative position $\vec{r}$ and relative

momentum $\vec{q}$ of the nucleon pair, in the rest frame of the deuteron, and R_+, R_-, P_+, P_- are their positions and momenta in that frame. Finally, $\mathcal{D}(\vec{r}, \vec{q})$ stands for the deuteron Wigner density,

$$\mathcal{D}(\vec{r}, \vec{q}) = \int d^3\xi e^{-i\vec{q}\cdot\vec{\xi}} \varphi_d\left(\vec{r} + \frac{\vec{\xi}}{2}\right)\varphi_d^*\left(\vec{r} - \frac{\vec{\xi}}{2}\right), \quad (3)$$

where φ_d is the deuteron wave function.

Hence, deuteron yield is given by the convolution of the deuteron Wigner function with the distributions (Wigner functions) of the protons and neutrons. Those distributions will be provided by our model, tuned on protons and pions. The actual Monte Carlo application will be explained in the next section.

Equation (1) allows one to better illustrate why the deuteron is a femtoscopic probe. For nuclear collisions, we will assume that the nucleon distributions vary with momentum much slower than the deuteron Wigner density, so that the integration over momentum difference in Eq. (2) is limited by $\mathcal{D}(\vec{r}, \vec{q})$.

If the homogeneity region for nucleons with given momentum is much larger than the typical spatial extension of the deuteron wave function, then the spatial integration in Eq. (2) covers the whole wave function. Due to its normalization, the whole integral tends to 1. In this case, deuteron production is equivalent to the production of one proton and one neutron, multiplied by the appropriate degeneracy factor.

On the other hand, if the emitting region is much smaller than the size of the deuteron wave function, then the integration in Eq. (2) is limited by $f_p \cdot f_n$ and gives a factor smaller than 1, representing just how much of the deuteron wave function is included. The interesting regime is where the size of the emitting region is just about the size of the deuteron, because this is when the former behavior changes into the latter.

Deuteron production thus becomes sensitive to the size of the emitting source and we want to use this dependence in our study.

III. THE MODEL

In the statistical (thermal) model, particle yields are given by the volume, temperature, and chemical potentials for the conserved charges. Together with spatial distributions of the emission points and the profile of the collective expansion velocity these are all ingredients that determine the so-called blast-wave (BW) model [57–59]. It will be extended here, however.

A. Freeze-out hypersurface

We parametrize the momentum of a particle with the help of transverse momentum p_t, transverse mass m_t, rapidity Y, and the azimuthal angle ϕ as

$$p^\mu = (m_t \cosh Y, p_t \cos\phi, p_t \sin\phi, m_t \sinh Y). \quad (4)$$

In this paper, we shall denote the rapidity with a capital letter in order to distinguish it from the spatial coordinate.

In the position space, we shall use the polar coordinates, r and the azimuthal angle Θ, in the transverse plane. Hyperbolic coordinates map the remaining two directions: the space-time rapidity

$$\eta_s = \frac{1}{2}\ln\left(\frac{t+z}{t-z}\right), \quad (5)$$

and the longitudinal proper time $\tau = \sqrt{t^2 - z^2}$. Then, one can write for the coordinates

$$x^\mu = (\tau \cosh\eta_s, r\cos\Theta, r\sin\Theta, \tau\sinh\eta_s). \quad (6)$$

When trying to simultaneously reproduce the identified p_t spectra and $v_2(p_t)$ of protons and pions, we found out that the usual formulation of the blast-wave model with the freeze-out along constant longitudinal proper time hyperbola is insufficient. Thus we replace it with the quadratic dependence of the freeze-out time on the radial coordinate,

$$\tau_f(r) = s_0 + s_2 r^2, \quad (7)$$

where s_0 and s_2 are parameters of the model.

The three-dimensional element of the freeze-out hypersurface is given by

$$d^3\Sigma_\mu = \varepsilon_{\mu\nu\kappa\rho}\frac{dx^\nu}{dr}\frac{dx^\kappa}{d\Theta}\frac{dx^\rho}{d\eta_s} dr\, d\Theta\, d\eta_s, \quad (8)$$

where $\varepsilon_{\mu\alpha\beta\gamma}$ is the Levi-Civita tensor.

Then, from Eq. (6) one gets

$$d^3\Sigma^\mu = \left(\cosh\eta_s, \frac{\partial\tau_f(r)}{\partial r}\cos\Theta, \frac{\partial\tau_f(r)}{\partial r}\sin\Theta, \sinh\eta_s\right) \times r\tau_f(r) d\eta_s dr\, d\Theta, \quad (9)$$

and Eq. (7) leads to

$$d^3\Sigma^\mu = (\cosh\eta_s, 2s_2 r\cos\Theta, 2s_2 r\sin\Theta, \sinh\eta_s) \times r\tau_f(r) d\eta_s dr\, d\Theta, \quad (10)$$

Note that Eqs. (6) and (9) just show how the positions in space and the freeze-out hypersurface are parametrized, respectively, with the help of coordinates. They do not yet describe the actual shape of the hot fireball.

We further extend the usual BW model to incorporate azimuthal anisotropies both in flow and spatial distribution. The radial size shows second-order oscillation around the mean R_0 with an amplitude $a_2 R_0$

$$R(\Theta) = R_0[1 - a_2\cos(2\Theta)]. \quad (11)$$

Technically, $R(\Theta)$ sets the maximum value that the coordinate r can attain. The azimuthal spatial anisotropy of the fireball is set by the Θ dependence of this maximum. The expansion velocity is parametrized as

$$u^\mu = (\cosh\eta_s \cosh\rho(r), \sinh\rho(r)\cos\Theta_b, \times \sinh\rho(r)\sin\Theta_b, \sinh\eta_s\cosh\rho(r)), \quad (12)$$

where the transverse rapidity grows linearly with (dimensionless) radial coordinate

$$\bar{r} = r/R(\Theta) \quad (13)$$

and exhibits an azimuthal oscillation parametrized by ρ_2

$$\rho(\bar{r}, \Theta_b) = \bar{r}\rho_0[1 + 2\rho_2\cos(2\Theta_b)], \quad (14)$$

with ρ_0 being the average transverse rapidity gradient. The velocity is directed along the angle $\Theta_b = \Theta_b(r, \Theta)$, which points in the direction perpendicular to the elliptical surface of the freeze-out,

$$\tan\left(\Theta_b - \frac{\pi}{2}\right) = \frac{dy}{dx} = \frac{\frac{dy}{d\Theta}}{\frac{dx}{d\Theta}}, \tag{15}$$

where the derivatives are taken along an $\bar{r} = \text{const}$ curve.

B. Momentum distribution

Along the freeze-out hypersurface, hadrons are produced according to the Cooper-Frye formula [60]

$$E\frac{d^3N}{dp^3} = \int_\Sigma d^3\Sigma \cdot p f(x, p), \tag{16}$$

where $f(x, p)$ is the distribution of the emission points in position and momentum space. Thermal production of deuterons is also calculated according to this formula.

In the simplest case, within the local rest frame of a moving fluid, $f(x, p)$ is assumed to be a Bose-Einstein or Fermi-Dirac distribution (or their Boltzmann approximation) [57,58].

Nevertheless, if the freeze-out happens from a viscous medium, that distribution must be modified [61]. Here, we adopt the parametrization of [62] which is based on the approach of [63]. It consists of modifying the momenta, temperature, and the chemical potential term in the original statistical distribution. The distribution for particles with mass m_n, baryon number b_n, and spin degeneracy g_n at temperature T then becomes

$$f^{\text{PTM}}_{\text{eq},n} = \frac{Z_n g_n}{\exp\left[\frac{\sqrt{\boldsymbol{p}'^2 + m_n^2}}{T + \beta_\Pi^{-1}\Pi\mathcal{F}} - b_n\left(\alpha_B + \frac{\Pi\mathcal{G}}{\beta_\Pi}\right)\right] + \Theta_n}, \tag{17}$$

where α_B is the ratio of baryon chemical potential to temperature, μ_B/T, and Θ_n is 1 (-1) for fermions (bosons). Other terms and symbols are explained in Appendix.

For the actual generation of hadrons we have adopted the hadron sampler from the SMASH package [64,65]. The original viscous corrections implemented there have been replaced by Eq. (17), because in the original formulation the corrections may outgrow the main term.

Resonance production is included in our model and SMASH was used to simulate their decays. However, subsequent rescatterings of hadrons were forbidden.

Chemical potentials for the hadrons at freeze-out have been assumed according to the partial chemical equilibrium scenario [66]. The chemical freeze-out is assumed to happen at the temperature 156 MeV [67], but the hadronic system stays together longer and cools down until it reaches the thermal freeze-out. In partial chemical equilibrium, this leads to the appearance of proper chemical potentials for all stable hadrons. Chemical potentials for resonances are determined from the condition that their production and decay keeps them in equilibrium with ground state hadrons. The chemical potentials then depend on temperature. In general, at the chemical freeze-out they coincide with the values determined in chemical equilibrium and then they grow as the temperature decreases. We took their values from [67].

C. Coalescence

Nucleons generated by the above procedure may subsequently couple to form a deuteron. In the simulation, this is implemented with the following steps [20]:

(i) We consider protons and neutrons at the place of their last interaction with the fireball or where their parent resonance decayed (i.e., their freeze-out).
(ii) For each p-n pair, the momentum and position of the proton and neutron are boosted to the center-of-mass frame of the pair.
(iii) The particle that has decoupled earlier is propagated to the time when the other particle was created.
(iv) We calculate the relative momentum $\Delta p = |\boldsymbol{p_1} - \boldsymbol{p_2}|$ and the relative distance $\Delta r = |\boldsymbol{r_1} - \boldsymbol{r_2}|$ at equal times of the p-n pair in their center-of-mass frame.
(v) To create a deuteron, we require that $\Delta p < \Delta p_{\text{max}}$ and $\Delta r < \Delta r_{\text{max}}$.
(vi) Next, the statistical spin and isospin factor 3/8 due to the spin and isospin projection to the deuteron state (probability $1/2 \times 3/4 = 3/8$) is added.
(vii) Finally, the chosen p-n pair is marked as a deuteron and its proton and neutron are removed from the list of created hadrons.

D. Model calibration

Let us recall our goal, which is to test if the two potential production mechanisms for deuterons can be discriminated by their prediction for $v_2(p_t)$. The p_t spectra of deuterons must be reproduced, but we do not aim at any resolving power here, for the production mechanism.

In this study we plan to calculate v_2 for one semicentral, one mid-central, and one peripheral centrality class. Data on $v_2(p_t)$ of deuterons were published in [68] for centrality classes 0–5%, 5–10%, 10–20%, 20–30%, 30–40%, 40–50%. We chose 0–5% and 30–40% for the comparison with data and 50–60% for a prediction, where the effects may be strongest due to higher degree of anisotropy, even though no experimental data are available there.

Unfortunately, the p_t spectra of deuterons have been published in different classes of centrality: 0–10%, 10–20%, 20–40% [68]. We will take this into account when simulating them.

For each centrality class, parameters of our model are tuned on p_t spectra and $v_2(p_t)$ for protons and pions. The spectra were published in [69] and the v_2 in [70], and they were divided into centrality classes that overlap with $v_2(p_t)$ for deuterons in [68].

Proceeding with the calibration of the model we note that the azimuthally integrated p_t spectra do not depend on the anisotropy parameters a_2 and ρ_2. This allows us to set the temperature T and transverse flow, parametrized with ρ_0, from the comparison to p_t spectra of identified hadrons. As a matter of fact, we use here the results of [71] where spectra of pions,

TABLE I. The parameters used for the generation of pions, protons, neutrons and direct deuterons from the hadron sampler for centrality classes 0–5%, 30–40%, and 50–60%.

Centrality	T (MeV)	η_f	R_0 (fm)	s_0 (fm/c)	a_2	ρ_2
0–5%	95	0.98	15.0	21 ± 2	0.016	0.008
30–40%	106	0.91	10.0	9 ± 1	0.085	0.03
50–60%	118	0.80	6.0	6 ± 0.5	0.15	0.02

kaons, (anti)protons, and Λ's were fitted simultaneously. For later simulations we use the centrality classes 0–5%, 30–40%, 50–60%. The transverse size parameter R_0 is taken from [72] and s_0 is determined so that the normalization of the p_t spectra comes out correct. The adopted parameters are listed in Table I.

The differential v_2 then depends on spatial anisotropy parameter a_2 and flow anisotropy ρ_2, This dependence is also different for protons and for pions [59]. Hence, the combination of proton and pion $v_2(p_t)$ allows us to set both a_2 and ρ_2 uniquely.

Figure 1 illustrates for centrality 30–40% the χ^2 that we have obtained when we compared a few calculated $v_2(p_t)$ of protons and pions for various values of a_2 and ρ_2 with data. Their anticorrelation is observed but we see that a best fit can be obtained.

At this point we observed that we are unable to reproduce $v_2(p_t)$ reasonably when we stick to the assumption that the freeze-out hypersurface is set by constant τ and does not depend on r. The reason is that $v_2(p_t)$ requires rather strong elliptic flow. Since ρ_0 parametrizes the transverse *rapidity*, the parts of the fireball at the edges move with velocities close to that of light. To see a sizable effect on the elliptic flow we need a variation in the transverse expansion *velocity*.

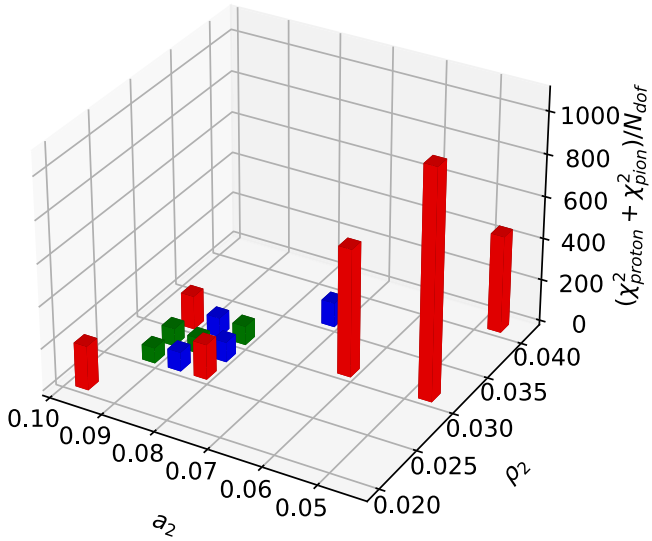

FIG. 1. The χ^2 from comparing theoretical results for various values of a_2 and ρ_2 with experimental data on $v_2(p_t)$ of protons and pions for the centrality class 30–40%.

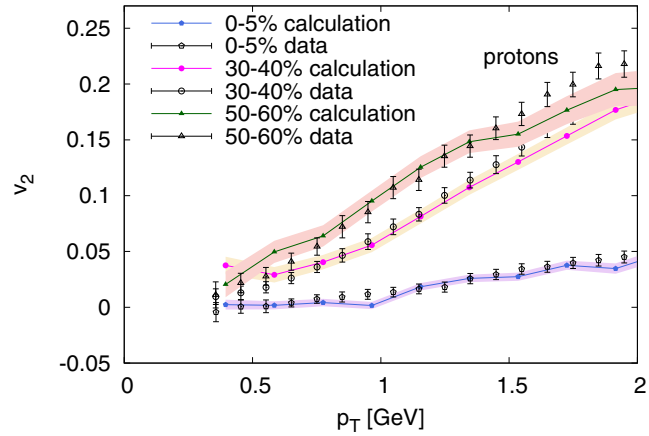

FIG. 2. Elliptic flow of protons for centrality classes 0–5%, 30–40%, and 50–60% compared to data from Pb+Pb collisions at $\sqrt{s_{NN}} = 2.76$ TeV by the ALICE Collaboration.

Close to the edge, the variation is rather limited since the expansion velocity is close to c and must remain below c, The effect of expansion velocity variation is enhanced if the freeze-out hypersurface bends downwards in the τ-r plane; i.e., regions which are farther from the longitudinal symmetry axis freeze out earlier.[1] Technically, this is expressed by the value $s_2 = -0.02$ fm^{-2}. The obtained anisotropy parameters for centrality classes in which we calculated $v_2(p_t)$ are listed in Table I.

The resulting $v_2(p_t)$ for protons and pions are plotted together with the experimental data in Figs. 2 and 3, respectively. This demonstrates that we tuned our parametrization well in order to reproduce the second-order anisotropy. In this paper we determined the v_2 with the event-plane method.

[1]The scenario is sometimes referred to as "burning log."

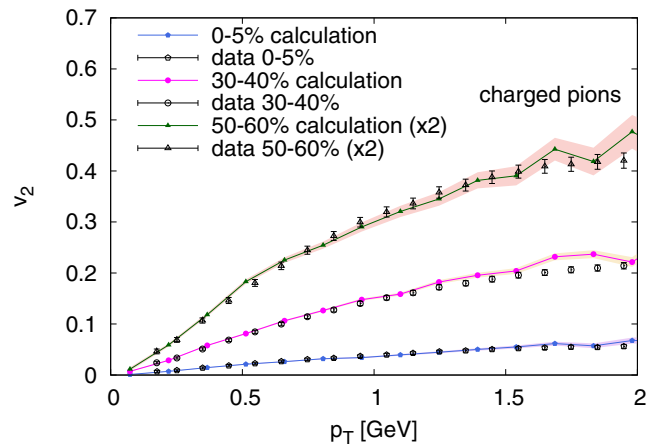

FIG. 3. Elliptic flow of pions for centrality classes 0–5%, 30–40%, and 50–60% compared to data from Pb+Pb collisions at $\sqrt{s_{NN}} = 2.76$ TeV by the ALICE Collaboration.

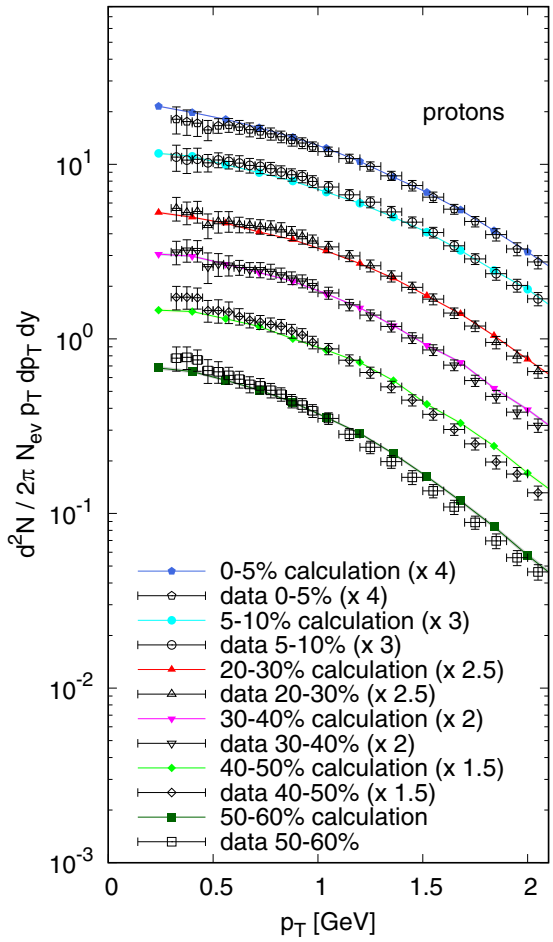

FIG. 4. Transverse momentum spectra of protons for centrality classes 0–5%, 5–10%, 20–30%, 30–40%, 40–50%, and 50–60% compared to data from Pb+Pb collisions at $\sqrt{s_{NN}} = 2.76$ TeV by the ALICE Collaboration.

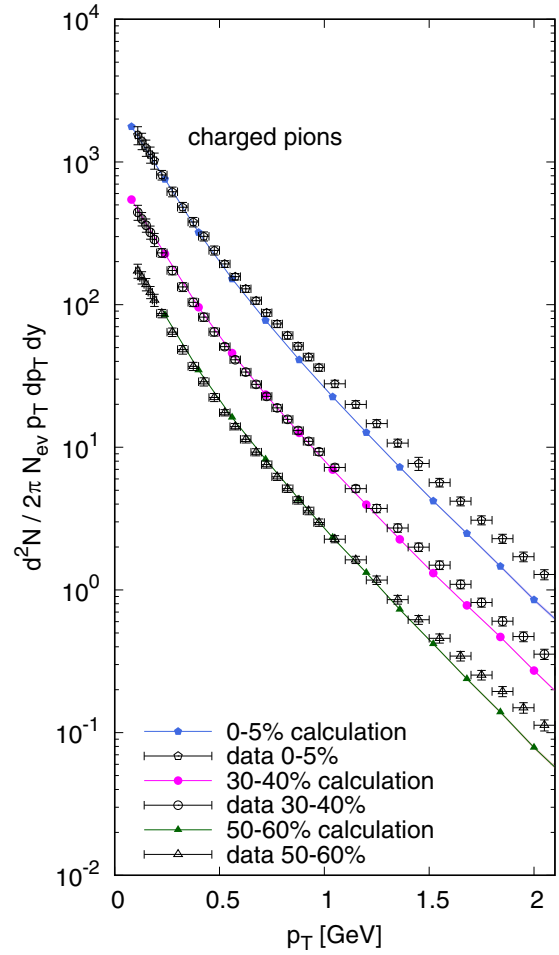

FIG. 5. Transverse momentum spectra of pions for centrality classes 0–5%, 30–40%, and 50–60% compared to data from Pb+Pb collisions at $\sqrt{s_{NN}} = 2.76$ TeV by the ALICE Collaboration.

The transverse momentum spectra of protons are shown in Fig. 4 and those of pions in Fig. 5. Since the deuteron p_t spectra are measured in wider centrality classes, we will simulate those by merging the results from both smaller centrality classes (e.g., 20–30% and 30–40% will be merged into 20–40% centrality class). To this end, we had to simulate also those classes which we do not use for the v_2 analysis. Figure 4 shows all resulting proton spectra. The parameters were determined in the same way as for the other centrality classes and are listed in Table II.

TABLE II. The parameters used for the generation of pions, protons, neutrons, and direct deuterons from the hadron sampler for centrality classes 5–10%, 20–30%, and 40–50%.

Centrality	T (MeV)	ρ_0	R_0 (fm)	s_0 (fm/c)
5–10%	97	0.97	13.0	17
20–30%	101	0.94	11.0	11
40–50%	112	0.86	7.0	7

IV. RESULTS AND DISCUSSION

After having constructed and calibrated the model it is now straightforward to simulate deuteron production. Thermal production is obtained just by using the mass and degeneracy factors of deuterons in the Cooper-Frye formula, Eq. (16). Coalescence was described in Sec. III C. The maximum distance of proton and neutron to form a deuteron was chosen as $\Delta r \leqslant 3.5$ fm, in accord with the investigation [20]. The correct yield is then obtained with $\Delta p \leqslant 0.26$ GeV.

For each centrality class, 10^6 events were initiated in the simulation chain. About 10% of them did not finish due to computational issues.

In Figs. 6 and 7 we present the transverse momentum spectra of deuterons produced thermally and by coalescence, respectively. At all investigated centralities, both models reproduce the yield (absolute normalisation of the spectra) and also the shape of the spectrum. Some discrepancies appear in thermally produced spectra, especially in noncentral collisions, where the simulated spectra are flatter than data. The similarities of results can be understood, since the product of f_p and f_n in Eq. (1) gives approximately the emission

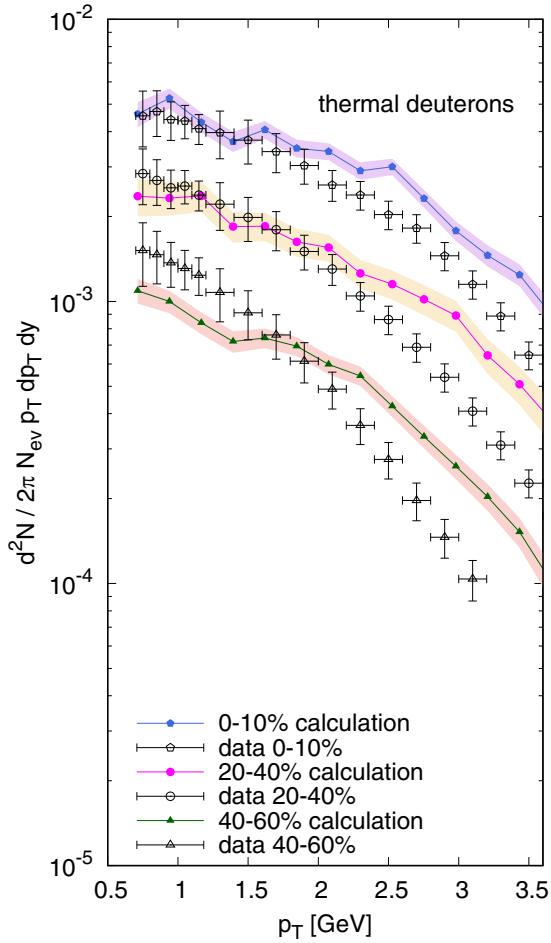

FIG. 6. Transverse momentum spectra of thermal deuterons for centrality classes 0–10%, 20–40%, and 40–60% compared with data from Pb+Pb collisions $\sqrt{s_{NN}} = 2.76$ TeV as measured by the ALICE Collaboration.

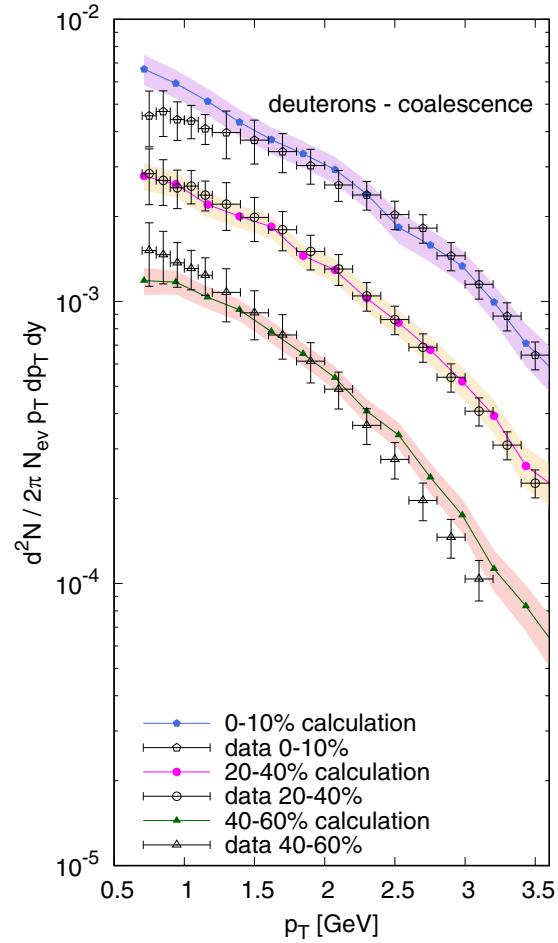

FIG. 7. Transverse momentum spectra of deuterons from coalescence for centrality classes 0–10%, 20–40%, and 40–60% compared with data from Pb+Pb collisions $\sqrt{s_{NN}} = 2.76$ TeV as measured by the ALICE Collaboration.

function of deuterons in the thermal model. The less detailed the observable that one looks at, the better is this rough argument.

Therefore, we look at the more detailed observable and examine the elliptic flow. In Fig. 8 the p_t dependence of v_2 is plotted. Experimental data are compared to both models used here. Recall that there in no room for tuning at this stage, since all parameters have been set by the comparison to protons and pions and the last two parameters have been fixed by deuteron spectra. Now, we see a clear difference between coalescence and thermal production. Generally, in noncentral collisions coalescence leads to higher elliptic flow than the statistical production. In the 20–30% centrality class it is the preferred model, particularly for p_t above 1.5 GeV. In central collisions, elliptic flow is almost zero and the simulation results are strongly affected by statistical fluctuations.

As we wanted to confirm our hypothesis that in more peripheral collisions coalescence may be more sensitive to the azimuthal variation of the homogeneity region, we looked at the 50–60% centrality class. This is just one decile beyond the coverage by experimental data and we suppose that it could be covered with better experimental statistics. Here, the difference between coalescence and the thermal model prediction is clear, beyond the applied error bars.

The elliptic flow—being actually the measure of transverse flow anisotropy—is larger from coalescence, when the size of the homogeneity region from which the deuterons come varies just around the size of the deuteron. The yield from coalescence is very sensitive to the interplay of these two sizes. Hence, one might expect that the anisotropy will be very sensitive to the spatial deuteron size, which is effectively set by Δr, here. Such a dependence might limit the robustness of our conclusions, since Δr is one of our model parameters. In order to test this robustness, we run simulations in which we lowered the value of Δr and increased Δp so that the normalisation of the spectra stays unchanged. We decreased Δr by as much as 1 fm, but stayed conservative and did not go for lower values. The results for v_2 are plotted in Fig. 9 for the 30–40% centrality class. As the size of the deuterons is effectively lowered, they become less sensitive to the variation of the homogeneity lengths and the anisotropy of the deuteron distribution—measured by v_2—decreases. With the

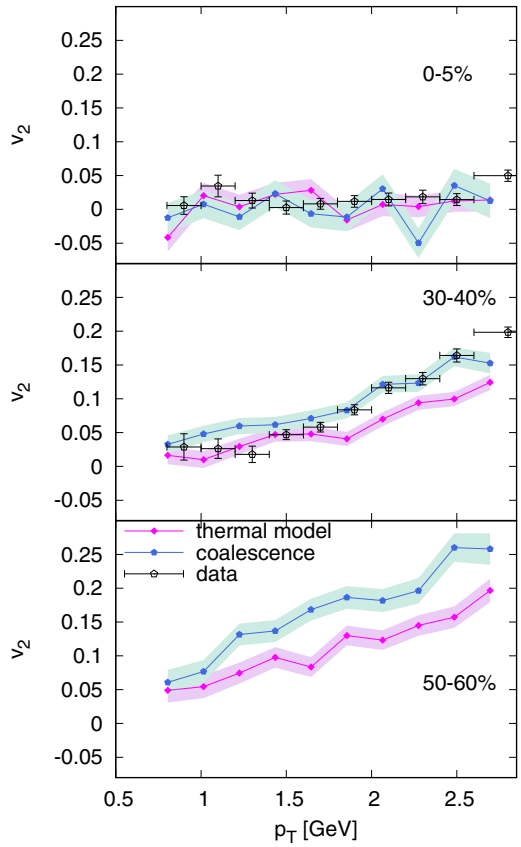

FIG. 8. Elliptic flow coefficient v_2 calculated for thermal production as well as coalescence for centrality classes 0–5%, 30–40%, and 50–60%, and compared to data from Pb+Pb collisions at $\sqrt{s_{NN}} = 2.76$ TeV, as measured by the ALICE Collaboration.

current variation of Δr the decrease is such that all obtained curves for v_2 stay close to experimental data. We stick to our conclusion that coalescence leads to larger v_2 than the thermal production.

We stressed several times, already, that for the yield from coalescence the size of the effective homogeneity region (also

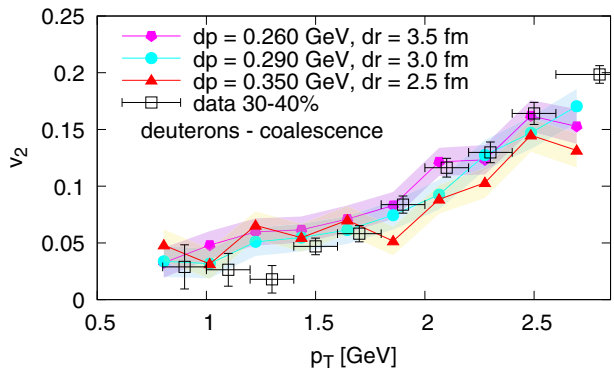

FIG. 9. Elliptic flow of deuterons from coalescence for different values of Δr and Δp, compared to experimental data from Pb+Pb collisions at $\sqrt{s_{NN}} = 2.76$ TeV, as measured by the ALICE Collaboration.

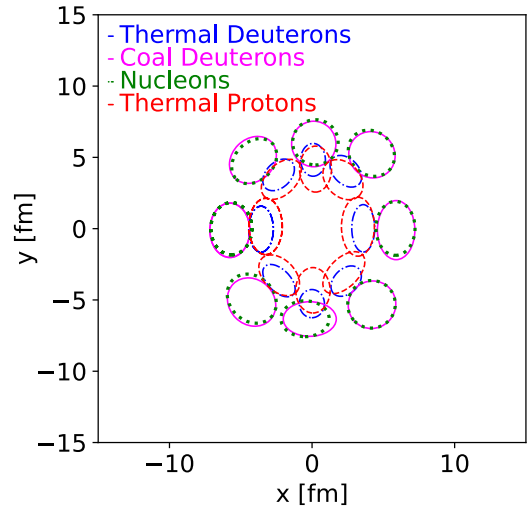

FIG. 10. Variances of the homogeneity regions that produce protons with $p_t \approx 1$ GeV and deuterons with $p_t \approx 2$ GeV, divided into eight bins by azimuthal angle of the momentum. Centrality class is 50–60%. The ellipses are centered around mean position of emission of given sort of particles and their half-axes are given by the variances of the emission points. We plot thermal protons (red dashed line), thermal deuterons (blue dash-dotted line), all nucleons that merge into deuterons via coalescence (green dotted line), and deuterons from coalescence (purple solid line).

known as homogeneity length) in comparison to the deuteron size is decisive. In order to explore this issue, we want to have a look at the homogeneity lengths in Fig. 10. We examine the centrality class 50–60%, so that the anisotropy is clearly visible, and focus on deuterons with p_t from the interval 2.0 ± 0.2 GeV and protons with p_t from the interval 1.0 ± 0.1 GeV. They are divided into eight bins of azimuthal angle of their momentum. For each type of particles we recorded the positions from which they were emitted. For deuterons from coalescence this means that we record the position where we calculate that the nucleon pair merged into the deuteron. From the obtained samples of emission points we determine the mean positions and the variances in the outward direction and in the direction perpendicular to it. Then, we draw ellipses with centers given by the mean emission position and the half-axes given by the variances. Thus, the ellipses represent the information about the homogeneity regions and lengths.

Figure 10 reveals an important insight: the intuitive picture based on the thermal production from the fireball must be modified, because some of the nucleons comes from decays of resonances. This shows up as a shift of the production region in the outward direction. For nucleons, the shift is about 2.5 fm. This shift has an impact on the emission region of the deuterons. Those from coalescence are produced also from nucleons that stem from resonance decays. Their emission region coincides with that of all nucleons. On the other hand, statistical production of deuterons does not include resonance decays. As a consequence, the source of statistically produced deuterons must fit into the thermal fireball. Due to higher mass of the deuterons with respect to protons, the thermal source of deuterons is smaller than that of protons and it

is pushed further towards the edge of the fireball. It might be interesting to explore the sizes of the emitting regions with the help of femtoscopy, as recently proposed in [45,46]. Figure 10 confirms that such a study may indeed also help with the discrimination of the potential deuteron production mechanism.

V. CONCLUSIONS

We conclude that the second-order azimuthal anisotropy of deuterons, also known as elliptic flow v_2, is larger in the case of coalescence than it is for the direct statistical production of deuterons. Our claim is based upon simulation with a carefully calibrated model that is fixed by reproducing the available data on proton and pion transverse momentum spectra and v_2.

Let us recall the important features of our approach which support the robustness of our conclusions:

(i) Our simulations include the decays of resonances.
(ii) We employ a fully developed parametrization of the emission and overcome numerical difficulties with integrating of the emission function by Monte Carlo sampling of the events, so that all details of source shape and flow are included.
(iii) We acknowledge that there are two potential causes for azimuthal anisotropy of hadron distribution: anisotropic shape of the fireball and the anisotropy of its expansion. We include them both and tune them via comparison to proton and pion $v_2(p_t)$.
(iv) We insist on reproduction of proton (nucleon) and pion data for p_t spectra and v_2. In the hadronic fireball, these are the most abundant species, and the former interact through the exchange of the latter. Hence, they form together the bulk of the fireball, and deuterons can be produced when this bulk of nucleons and pions decouples.

On the other hand, we remained on a simpler level with the modeling of the deuteron wave function. In general, any model wave function of the deuteron will include its size and so we expect that our results will stay qualitatively valid with any of them. The study [43] has shown the sensitivity of the calculated deuteron yield to the model for the wave function that is used, albeit with rather simple modeling of the source. It will be very interesting, though beyond our scope in this paper, to try other models for the deuteron wave function with this approach.

Note that another use of the blast-wave model to reproduce elliptic flow has been documented in literature [5,53,54]. To achieve this, azimuthal variation of the transverse expansion velocity of the bulk was implemented with dependence on the p_t of the produced particle. This may mimic continuous freeze-out as it naturally occurs in transport models. In our work, we stayed strictly within the framework of the blast-wave model, which assumes common freeze-out for all hadrons. We showed that it is possible to reproduce deuteron spectra and elliptic flow within these constraints.

The method of using v_2 for the distinction between coalescence and statistical production makes use of the homogeneity lengths that vary with the azimuthal angle of the emission. It may work if the homogeneity lengths are comparable to or smaller than the size of the deuteron, otherwise we would expect similar v_2 from both production mechanisms. Hence, the method should work best in collisions with larger impact parameter when the spatial anisotropy can be largest. Whether it works as well in collisions of smaller systems, when the homogeneity lengths are always smaller than the typical size of the deuteron wave function, remains to be studied.

It may appear as an attractive idea to apply the same kind of study on v_2 of larger clusters, since their wave functions have different sizes and may be more sensitive to the azimuthal variation of the homogeneity lengths. On the other hand, the applicability of the method will be limited by the available statistics. This idea remains to be studied, as well.

ACKNOWLEDGMENTS

This project is supported by the Czech Science Foundation (GAČR) under Grant No. 22-25026S. B.T. acknowledges support from VEGA 1/0521/22. Computational resources were provided by the e-INFRA CZ project (ID:90254), supported by the Ministry of Education, Youth and Sports of the Czech Republic. We thank N. Götz for the assistance with setting SMASH.

APPENDIX: THE MODIFIED DISTRIBUTION OF PARTICLE MOMENTA

Here we explain the symbols that appear in the modified momentum distribution displayed in Eq. (17). Note that it accounts for the departure of the distribution from the perfect-fluid equilibrium case due nonvanishing gradients. We chose this version of correction because it is more robust than the method of adding correction terms [61] which may make the resulting distribution negative for too large momenta. We closely follow here the formalism of [62].

For later reference, we start with some definitions and preliminaries.

1. Definitions

To keep the notation less cumbersome, we use $a \cdot b$ for the scalar product of two four-vectors ($a \cdot b = a_\mu b^\mu$) and also for multiplication with tensors (e.g., $a \cdot t \cdot b = t^{\mu\nu} a_\mu b_\nu$). Transverse projector to velocity is defined as

$$\Delta^{\mu\nu} = g^{\mu\nu} - u^\mu u^\nu, \tag{A1}$$

and the projector for tensors as

$$\Delta^{\mu\nu}_{\alpha\beta} = \tfrac{1}{2}\left(\Delta^\mu_\alpha \Delta^\nu_\beta + \Delta^\mu_\beta \Delta^\nu_\alpha\right) - \tfrac{1}{3}\Delta^{\mu\nu}\Delta_{\alpha\beta}. \tag{A2}$$

With its help, one can define the velocity shear tensor

$$\sigma_{\mu\nu} = \Delta^{\alpha\beta}_{\mu\nu}\partial_\beta u_\alpha. \tag{A3}$$

The fluid local rest frame (LRF) is the one in which spatial components of u^μ vanish. In LRF, the three spatial dimensions can be spanned by three unit vectors X_i. These vectors can be boosted to any other reference frame and their components will be X_i^μ. With their help, one can project out from four-vectors their components, which make up the spatial

components in LRF,

$$w_i = X_i^\mu w_\mu, \tag{A4}$$

and similarly for tensors,

$$t_{ij} = X_i^\mu X_j^\nu t_{\mu\nu}. \tag{A5}$$

The locally equilibrated distribution function for species n is the standard Bose-Einstein of Fermi-Dirac distribution,

$$f_{\mathrm{eq},n}(x,p) = \frac{g_n}{\exp\left(\frac{p\cdot u(x)}{T(x)} - \alpha_n(x)\right) + \Theta_n}. \tag{A6}$$

Recall that g_n is the spin degeneracy, $\alpha_n(x) = \mu_n(x)/T(x)$, and $\Theta_n = 1\,(-1)$ for fermions (bosons). One also defines

$$\bar{f}_{\mathrm{eq},n} = 1 - g_n^{-1}\Theta_n f_{\mathrm{eq},n}. \tag{A7}$$

A shorthand is introduced for thermal integrals of species n,

$$J_{kq,n} = \int \frac{d^3p}{(2\pi)^3 E} \frac{(u\cdot p)^{k-2q}(-p\cdot\Delta\cdot p)^q}{(2q+1)!!} f_{\mathrm{eq},n}\bar{f}_{\mathrm{eq},n}, \tag{A8}$$

and they are summed over all species in

$$\mathcal{J}_{kq} = \sum_n J_{kq,n}, \tag{A9}$$

$$\mathcal{N}_{kq} = \sum_n b_n J_{kq,n}, \tag{A10}$$

$$\mathcal{M}_{kq} = \sum_n b_n^2 J_{kq,n}. \tag{A11}$$

The energy density and the net baryon density in equilibrium are

$$\mathcal{E} = \sum_n \int \frac{d^3p}{(2\pi)^3 E}(u\cdot p)^2 f_{\mathrm{eq},n}, \tag{A12}$$

$$n_B = \sum_n b_n \int \frac{d^3p}{(2\pi)^3 E}(u\cdot p) f_{\mathrm{eq},n}, \tag{A13}$$

and the equilibrium pressure

$$\mathcal{P}_{\mathrm{eq}} = \frac{1}{3}\sum_n \int \frac{d^3p}{(2\pi)^3 E}(-p\cdot\Delta\cdot p) f_{\mathrm{eq},n}. \tag{A14}$$

We shall also use the following temperature-dependent coefficients:

$$\mathcal{G} = T\frac{(\mathcal{E}+\mathcal{P}_{\mathrm{eq}})\mathcal{N}_{20} - n_B\mathcal{J}_{30}}{\mathcal{J}_{30}\mathcal{M}_{10} - \mathcal{N}_{20}^2}, \tag{A15}$$

$$\mathcal{F} = T^2\frac{n_B\mathcal{N}_{20} - (\mathcal{E}+\mathcal{P}_{\mathrm{eq}})\mathcal{M}_{10}}{\mathcal{J}_{30}\mathcal{M}_{10} - \mathcal{N}20^2}. \tag{A16}$$

2. The formula for the momentum distribution

Now we can explain the formula Eq. (17), which we repeat here for convenience:

$$f_{\mathrm{eq},n}^{\mathrm{PTM}} = \frac{Z_n g_n}{\exp\left[\frac{\sqrt{\boldsymbol{p}'^2 + m_n^2}}{T + \beta_\Pi^{-1}\Pi\mathcal{F}} - b_n\left(\alpha_B + \frac{\Pi\mathcal{G}}{\beta_\Pi}\right)\right] + \Theta_n}, \tag{A17}$$

The thermal distribution works with the momentum $\boldsymbol{p}'$. It is related to the momentum in the local rest frame (LRF) $\boldsymbol{p}$ through

$$p_i = A_{ij}p'_j - q_i\sqrt{\boldsymbol{p}'^2 + m_n^2} + b_n T a_i, \tag{A18}$$

where

$$A_{ij} = \left(1 + \frac{\Pi}{3\beta_\Pi}\right)\delta_{ij} + \frac{\pi_{ij}}{2\beta_\pi}, \tag{A19}$$

$$q_i = \frac{V_{B,i} n_B T}{\beta_V(\mathcal{E}+\mathcal{P}_{eq})}, \tag{A20}$$

$$a_i = \frac{V_{B,i}}{\beta_V}. \tag{A21}$$

For the bulk viscous pressure and the shear stress tensor we assume the Navier-Stokes form

$$\Pi = -\zeta\,\partial_\mu u^\mu, \tag{A22}$$

$$\pi^{\mu\nu} = 2\eta\sigma^{\mu\nu}, \tag{A23}$$

nevertheless, in our application we set the bulk viscosity identically 0. For the shear viscosity we assume $\eta/s = 0.2$. The LRF spatial components of shear stress are $\pi_{ij} = X_i^\mu X_j^\nu \pi_{\mu\nu}$. The Navier-Stokes expression for the baryon current would be

$$V_B^\mu = \kappa_B \Delta^{\mu\nu}\partial_\nu\left(\frac{\mu(x)}{T(x)}\right), \tag{A24}$$

with $\kappa_B = T\sigma_B$ and σ_B is the baryon conductivity. Then, $V_{B,i} = X_i^\mu V_{B,\mu}$ is its spatial component in the LRF. Nevertheless, our density profile and temperature do not vary with the coordinates and so the baryon current vanishes.

Out of the ratios of bulk viscosity, baryon diffusion coefficient, and shear viscosity to the relaxation time—β_Π, β_V, and β_π—we thus do not need the former two. The third one is determined as

$$\beta_\pi = \frac{\mathcal{J}_{32}}{T}. \tag{A25}$$

The factor Z_n normalizes the distribution to fix the particle density. It is chosen as [62]

$$Z_n = \frac{1}{\det A}\frac{n_n^{(1)}}{n_{\mathrm{eq},n}\left(T + \beta_\pi^{-1}\Pi\mathcal{F}, \alpha_B + \beta_\Pi^{-1}\Pi\mathcal{G}\right)}, \tag{A26}$$

where $n_{\mathrm{eq},n}(T,\alpha)$ is the equilibrium particle density and

$$n_n^{(1)} = n_{\mathrm{eq},n} + \frac{\Pi}{\beta_\Pi}\left(n_{\mathrm{eq},n} + b_n J_{10,n}\mathcal{G} + \frac{J_{20,n}\mathcal{F}}{T^2}\right). \tag{A27}$$

Nevertheless, since we do not have the bulk viscous pressure in our simulations, the normalization simplifies to just

$$Z_n = \frac{1}{\det A}. \tag{A28}$$

[1] H. Agakishiev *et al.* (STAR Collaboration), Nature (London) **473**, 353 (2011); **475**, 412(E) (2011).
[2] J. Adam *et al.* (STAR Collaboration), Nat. Phys. **16**, 409 (2020).
[3] A. Andronic, P. Braun-Munzinger, K. Redlich, and J. Stachel, Nature (London) **561**, 321 (2018).
[4] A. Andronic, P. Braun-Munzinger, K. Redlich, and J. Stachel, J. Phys.: Conf. Ser. **779**, 012012 (2017).
[5] L. Zhu, H. Zheng, C. M. Ko, and Y. Sun, Eur. Phys. J. A **54**, 175 (2018).
[6] L. Adamczyk *et al.*, Phys. Rev. C **94**, 034908 (2016).
[7] S. T. Butler and C. A. Pearson, Phys. Rev. **129**, 836 (1963).
[8] H. H. Gutbrod, A. Sandoval, P. J. Johansen, A. M. Poskanzer, J. Gosset, W. G. Meyer, G. D. Westfall, and R. Stock, Phys. Rev. Lett. **37**, 667 (1976).
[9] H. Sato and K. Yazaki, Phys. Lett. B **98**, 153 (1981).
[10] M. Gyulassy, K. Frankel, and E. A. Remler, Nucl. Phys. A **402**, 596 (1983).
[11] L. P. Csernai and J. I. Kapusta, Phys. Rep. **131**, 223 (1986).
[12] S. Mrówczyński, J. Phys. G **13**, 1089 (1987).
[13] V. L. Lyuboshits, Yad. Fiz. **48**, 1501 (1988) [Sov. J. Nucl. Phys. **48**, 956 (1988)].
[14] R. Scheibl and U. W. Heinz, Phys. Rev. C **59**, 1585 (1999).
[15] G. Chen, Y. L. Yan, D. S. Li, D. M. Zhou, M. J. Wang, B. G. Dong, and B. H. Sa, Phys. Rev. C **86**, 054910 (2012).
[16] G. Chen, H. Chen, J. Wu, D. S. Li, and M. J. Wang, Phys. Rev. C **88**, 034908 (2013).
[17] K. J. Sun and L. W. Chen, Phys. Lett. B **751**, 272 (2015).
[18] Z. J. Dong, G. Chen, Q. Y. Wang, Z. L. She, Y. L. Yan, F. X. Liu, D. M. Zhou, and B. H. Sa, Eur. Phys. J. A **54**, 144 (2018).
[19] K. J. Sun, L. W. Chen, C. M. Ko, J. Pu, and Z. Xu, Phys. Lett. B **781**, 499 (2018).
[20] S. Sombun, K. Tomuang, A. Limphirat, P. Hillmann, C. Herold, J. Steinheimer, Y. Yan, and M. Bleicher, Phys. Rev. C **99**, 014901 (2019).
[21] P. Hillmann, K. Käfer, J. Steinheimer, V. Vovchenko, and M. Bleicher, J. Phys. G **49**, 055107 (2022).
[22] S. Mrówczyński, Acta Phys. Pol. B **48**, 707 (2017).
[23] P. Danielewicz and G. F. Bertsch, Nucl. Phys. A **533**, 712 (1991).
[24] D. Oliinychenko, L. G. Pang, H. Elfner, and V. Koch, Phys. Rev. C **99**, 044907 (2019).
[25] J. Staudenmaier, D. Oliinychenko, J.M. Torres-Rincon, and H. Elfner, Phys. Rev. C **104**, 034908 (2021).
[26] S. Mrówczyński, Eur. Phys. J. Spec. Top. **229**, 3559 (2020).
[27] J. Aichelin, E. Bratkovskaya, A. Le Fèvre, V. Kireyeu, V. Kolesnikov, Y. Leifels, V. Voronyuk, and G. Coci, Phys. Rev. C **101**, 044905 (2020).
[28] S. Gläßel, V. Kireyeu, V. Voronyuk, J. Aichelin, C. Blume, E. Bratkovskaya, G. Coci, V. Kolesnikov, and M. Winn, Phys. Rev. C **105**, 014908 (2022).
[29] V. Kireyeu, J. Steinheimer, J. Aichelin, M. Bleicher, and E. Bratkovskaya, Phys. Rev. C **105**, 044909 (2022).
[30] G. Coci, S. Gläßel, V. Kireyeu, J. Aichelin, C. Blume, E. Bratkovskaya, V. Kolesnikov, and V. Voronyuk, Phys. Rev. C **108**, 014902 (2023).
[31] V. Kireyeu, G. Coci, S. Glaessel, J. Aichelin, C. Blume, and E. Bratkovskaya, arXiv:2304.12019.
[32] R. Wang, Y. G. Ma, L. W. Chen, C. M. Ko, K. J. Sun, and Z. Zhang, Phys. Rev. C **108**, L031601 (2023).
[33] S. Mrówczyński, Phys. Lett. B **248**, 459 (1990).
[34] S. Mrówczyński, Phys. Lett. B **277**, 43 (1992).
[35] S. Mrówczyński, Phys. Lett. B **308**, 216 (1993).
[36] K. Blum and M. Takimoto, Phys. Rev. C **99**, 044913 (2019).
[37] M. Kachelrieß, S. Ostapchenko, and J. Tjemsland, Eur. Phys. J. A **56**, 4 (2020).
[38] M. Kachelrieß, S. Ostapchenko, and J. Tjemsland, Eur. Phys. J. A **57**, 167 (2021).
[39] M. Kachelrieß, S. Ostapchenko, and J. Tjemsland, Phys. Rev. C **108**, 024903 (2023).
[40] M. Kachelrieß, S. Ostapchenko, and J. Tjemsland, Comput. Phys. Commun. **287**, 108698 (2023).
[41] F. Bellini and A. P. Kalweit, Phys. Rev. C **99**, 054905 (2019).
[42] F. Bellini, K. Blum, A. P. Kalweit, and M. Puccio, Phys. Rev. C **103**, 014907 (2021).
[43] M. Mahlein, L. Barioglio, F. Bellini, L. Fabbietti, C. Pinto, B. Singh, and S. Tripathy, Eur. Phys. J. C **83**, 804 (2023).
[44] S. Bazak and S. Mrówczyński, Eur. Phys. J. A **56**, 193 (2020).
[45] S. Mrówczyński and P. Słoń, Acta Phys. Pol. B **51**, 1739 (2020).
[46] S. Mrówczyński and P. Słoń, Phys. Rev. C **104**, 024909 (2021).
[47] S. Acharya *et al.* (ALICE Collaboration), Phys. Lett. B **819**, 136440 (2021).
[48] S. Acharya *et al.* (ALICE Collaboration), Phys. Rev. Lett. **131**, 042301 (2023).
[49] S. Mrówczynski, Acta Phys. Polon. B **55**, 6-A2 (2024).
[50] Z. Fecková, J. Steinheimer, B. Tomášik, and M. Bleicher, Phys. Rev. C **93**, 054906 (2016).
[51] S. Acharya *et al.* (ALICE Collaboration), Phys. Rev. Lett. **131**, 041901 (2023).
[52] STAR Collaboration, arXiv:2304.10993.
[53] Y. Oh, Z. W. Lin, and C. M. Ko, Phys. Rev. C **80**, 064902 (2009).
[54] X. Yin, C. M. Ko, Y. Sun, and L. Zhu, Phys. Rev. C **95**, 054913 (2017).
[55] W. Zhao, L. Zhu, H. Zheng, C. M. Ko, and H. Song, Phys. Rev. C **98**, 054905 (2018).
[56] L. Zhu, C. M. Ko, and X. Yin, Phys. Rev. C **92**, 064911 (2015).
[57] E. Schnedermann, J. Sollfrank, and U. W. Heinz, Phys. Rev. C **48**, 2462 (1993).
[58] T. Csörgő and B. Lörstad, Phys. Rev. C **54**, 1390 (1996).
[59] B. Tomášik, Acta Phys. Pol. B **36**, 2087 (2005).
[60] F. Cooper and G. Frye, Phys. Rev. D **10**, 186 (1974).
[61] D. Teaney, Phys. Rev. C **68**, 034913 (2003).
[62] M. McNelis and U. Heinz, Phys. Rev. C **103**, 064903 (2021).
[63] S. Pratt and G. Torrieri, Phys. Rev. C **82**, 044901 (2010).
[64] J. Weil *et al.*, Phys. Rev. C **94**, 054905 (2016).
[65] A. Schäfer *et al.*, Eur. Phys. J. A **58**, 230 (2022).
[66] H. Bebie, P. Gerber, J. L. Goity, and H. Leutwyler, Nucl. Phys. B **378**, 95 (1992).
[67] I. Melo and B. Tomášik, J. Phys. G **47**, 045107 (2020).
[68] S. Acharya *et al.* (ALICE Collaboration), Eur. Phys. J. C **77**, 658 (2017).
[69] B. Abelev *et al.* (ALICE Collaboration), Phys. Rev. C **88**, 044910 (2013).
[70] B. B. Abelev *et al.* (ALICE Collaboration), J. High Energy Phys. 06 (2015) 190.
[71] I. Melo and B. Tomášik, J. Phys. G **43**, 015102 (2016).
[72] S. Chatterjee, B. Mohanty, and R. Singh, Phys. Rev. C **92**, 024917 (2015).